NANO LETTERS

pubs.acs.org/NanoLett Letter

Characterization of Orbital Angular Momentum Quantum States Empowered by Metasurfaces

Min Wang, Lieyu Chen, Duk-Yong Choi, Shuangyin Huang, Qiang Wang, Chenghou Tu, Hua Cheng, Jianguo Tian, Yongnan Li,* Shuqi Chen,* and Hui-Tian Wang*

Cite This: Nano Lett. 2023, 23, 3921−3928 Read Online

ABSTRACT: Twisted photons can in principle carry a discrete unbounded amount of orbital angular momentum (OAM), which are of great significance for quantum communication and fundamental tests of quantum theory. However, the methods for characterization of the OAM quantum states present a fundamental limit for miniaturization. Metasurfaces can exploit new degrees of freedom to manipulate optical fields beyond the capabilities of bulk optics, opening a broad range of novel and superior applications in quantum photonics. Here we present a scheme to reconstruct the density matrix of the OAM quantum states of single photons with all-dielectric metasurfaces composed of birefringent meta-atoms. We have also measured the Schmidt number of the OAM entanglement by the multiplexing of multiple degrees of freedom. Our work represents a step toward the practical application of quantum metadevices for the measurement of OAM quantum states in free-space quantum imaging and communications.

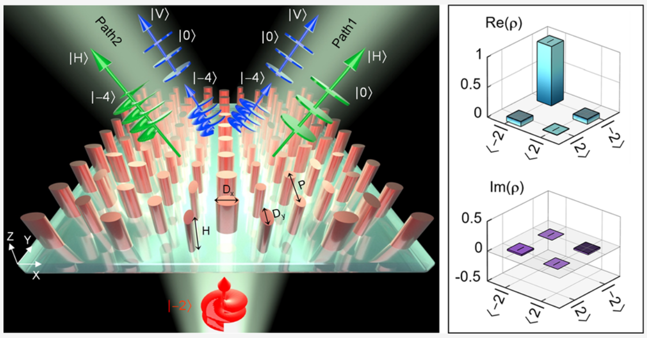

KEYWORDS: *metasurface, orbital angular momentum, polarization, entanglement, Schmidt number*

A metasurface with engineered subwavelength structures offers the possibility of replacing traditionally bulk optics with flat optics.[1−3] The manipulation of the light's wavefront with high transmittance can be effectively achieved by tailoring the parent material and sizes, shapes, and spatial arrangement of the subwavelength antenna array, based on all-dielectric platforms.[4−7] As promising compact and robust integrated optical devices, the metasurfaces have been widely used to enable optical applications, such as imaging,[8−11] holography,[12−15] optical cloaking,[16,17] and nonlinear optics.[18−20] Recently, the metasurfaces have crossed from the classical realm to the quantum realm to further upgrade the multifunctional integration capability of quantum technology.[21,22] Its first advantage is to generate and manipulate the entangled photon states, which are at the heart of the photonic quantum information. Benefiting from the multipath of a metalens array, a compact high-dimensional multiphoton quantum source has been achieved based on a spontaneous parametric down-conversion (SPDC) process in a nonlinear crystal.[23] The photonic spin−orbit interaction mechanism in the metasurface provides a way to generate entanglement between the spin and orbital angular momenta of photons.[24] Another quantum improvement is the measurement and reconstruction of quantum states. The interleaved metagratings perform quantum projections in a multiphoton Hilbert space to retrieve the polarization quantum state tomography.[25] Especially, the metasurface-based measurement of quantum states is associated with the multiplexing.[26−28]

As a fundamental degree of freedom of photons, orbital angular momentum (OAM) can offer an unbounded discrete basis to construct an arbitrarily large Hilbert space, which has the potential to increase channel capacity in many quantum protocols.[29−31] Conventionally, the methods for measurement of the OAMs include bulk optical components, for example spiral phase plates[32] and a *q*-plate[33−35] and a hologram in a spatial light modulator (SLM).[36−38] However, the reconstruction of the OAM quantum states based on these apparatuses potentially suffers from errors associated with the movement of bulk optics. Moreover, the sequential implementations of projective measurements by the SLM present a fundamental limit for miniaturization.[39] Here we demonstrate the measurement of the OAM states of photons using an all-dielectric metasurface with birefringent meta-atoms, which allows simultaneous and elaborate manipulation of the path, polarization, and OAM based on the on-demand propagation phase

Received: February 14, 2023
Revised: April 21, 2023
Published: April 27, 2023

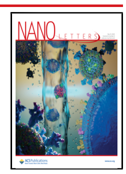

https://doi.org/10.1021/acs.nanolett.3c00554
Nano Lett. 2023, 23, 3921−3928

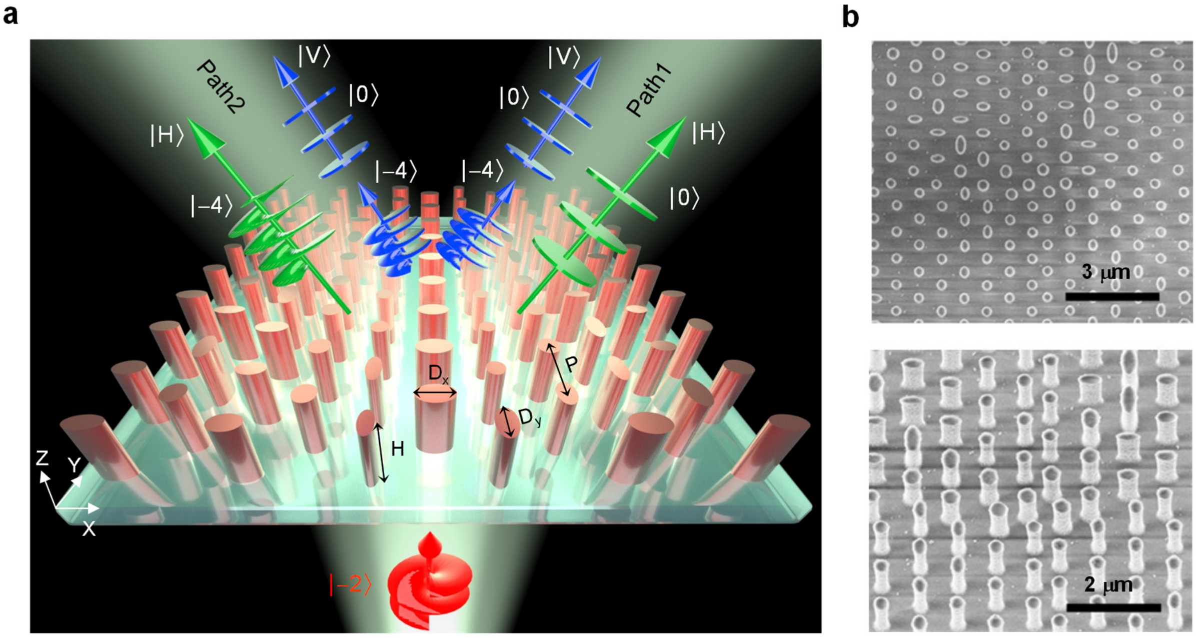

Figure 1. Concept of projection for the OAM state $|-2\rangle$ using a metasurface. (a) Sketch of a metasurface being used to diffract an input OAM state $|-2\rangle$ into Path1 and Path2 according to different polarization and OAM bases. For H-polarized light, the metasurface adding and subtracting two quanta of OAM in Path1 and Path2, respectively, projections on the states $|\pm 2\rangle$ are realized in the two paths when filtering the Gaussian mode with a single mode fiber. For V-polarized light, the metasurface does a superposition of adding and removing two quanta of OAM, with different phases in the two paths, so that $|-2\rangle$ is mapped into $|0\rangle + |-4\rangle$ in Path1 and into $|0\rangle + j|-4\rangle$ in Path2, which would be measured combined with a projection on $|0\rangle$ performed by the SMF. Other incident states can obviously have different projections. The other incident states can obviously be deduced to be a particular projection case. (b) Scanning electron microscopy images at the top and tilted views of a part of the fabricated metasurface. The period between the nanopillars is 850 nm in both directions.

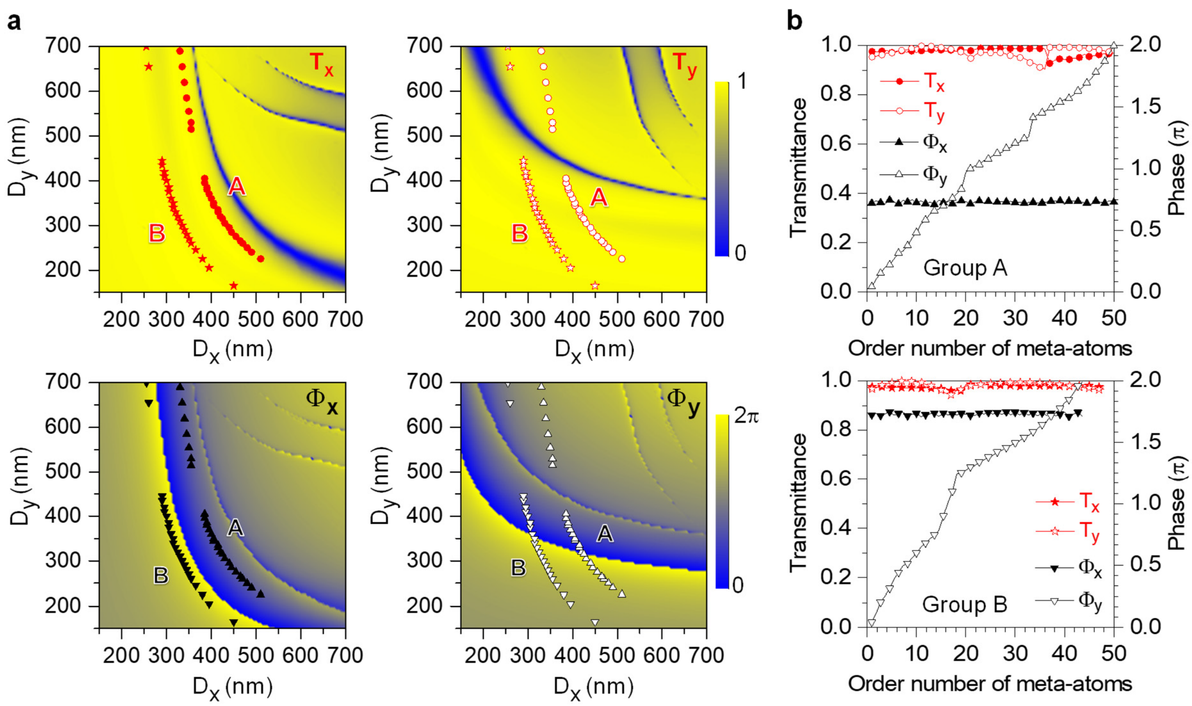

Figure 2. Design of the multiplexing metasurface. (a) Simulated transmittances (T_x and T_y) and phase shifts (Φ_x and Φ_y) as functions of D_x and D_y of the elliptical pillars for the x- and y-polarized light at a wavelength of 1550 nm when the elliptical-pillar array has a period of 850 nm and a height of 940 nm. (b) Transmittances and phase shifts of two groups (A and B) of the elliptical pillars with the same lattice.

of the elliptical nanopillars. The adoption of an all-dielectric configuration not only facilitates the integration with CMOS technology but also ensures the large size and high performance of the metadevices. By using the metasurface as the basis projector, we can reconstruct the density matrix of an arbitrary OAM state with high fidelity and measure the Schmidt number of the OAM entanglement. Our work indicates that the metasurface is suitable for the measurement

https://doi.org/10.1021/acs.nanolett.3c00554
Nano Lett. 2023, 23, 3921−3928

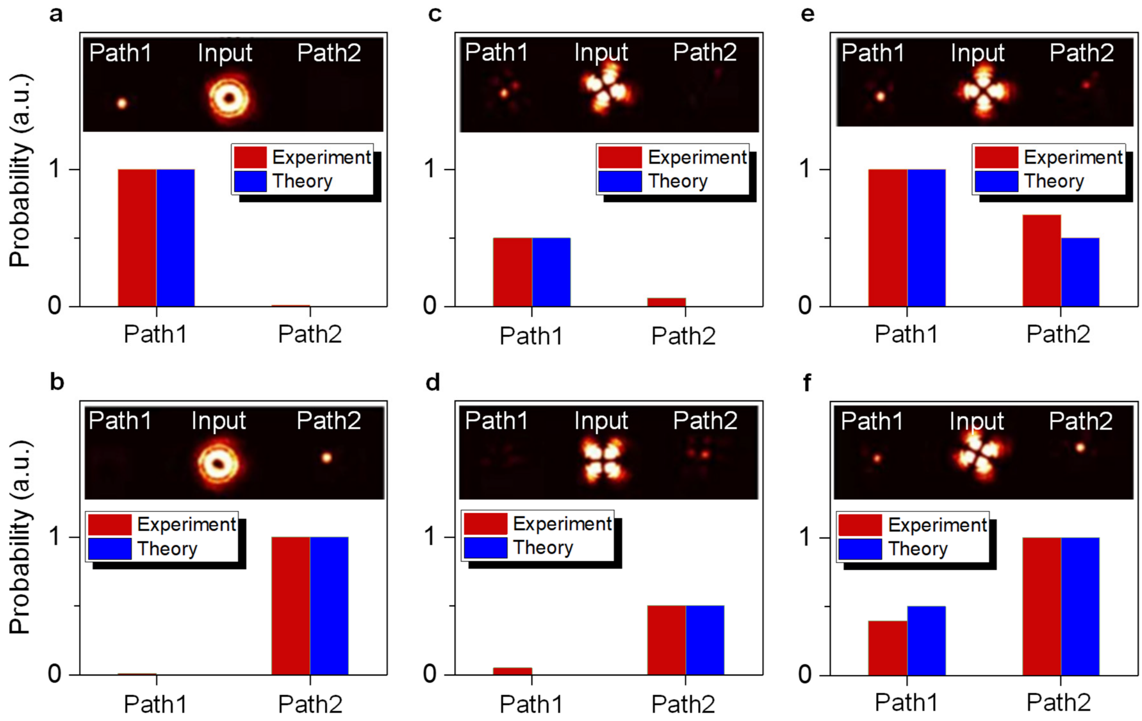

Figure 3. Characterization of the metasurface for the projection of OAM state. The theoretical and experimentally normalized detection probabilities of the Gaussian mode in Path1 and Path2 behind the metasurface for different input polarization and OAM states: (a) $|H\rangle|-2\rangle$, (b) $|H\rangle|+2\rangle$, (c) $|V\rangle|-J\rangle$, (d) $|V\rangle|-\rangle$, (e) $|V\rangle|+\rangle$, and (f) $|V\rangle|+J\rangle$. Insets: the corresponding diffracted patterns measured by CCD with a microscope lens with a magnification of 20× and a Fourier lens with a focal length of 75 mm.

of the OAM quantum states, which goes far beyond the conventional optics.

As is well-known, a Laguerre−Gaussian mode has a helical phase front of exp $(jm\varphi)$, where m can take any integer value and represents the quantum number of OAM per photon. For a given m, the OAM pure state evolves in the Hilbert space spanned by one basis $\{|+m\rangle,|-m\rangle\}$ and it can be described by one point on the Bloch sphere.[40] As an example, we take any OAM pure state $|\Psi\rangle$ with $|m| = 2$, which can be written as

$$|\Psi\rangle = \cos(\theta/2)|+2\rangle + e^{j\phi}\sin(\theta/2)|-2\rangle \quad (1)$$

where $|\pm 2\rangle$ indicate the OAM states, which refer to paraxial fields carrying OAMs of $\pm 2\hbar$ per photon, respectively. θ and ϕ are defined on the Bloch sphere: $\theta \in [0,2\pi]$ indicates the weighting factor, and $\phi \in [0, 2\pi]$ describes the relative phase between two superposition modes $|\pm 2\rangle$ (Figure S1).

To characterize the OAM quantum states $|\Psi\rangle$ with $|m| = 2$, we need to project it into different bases to access the coherence term of state superposition, including three sets of orthogonal bases $(|\pm 2\rangle, |\pm\rangle = (|+2\rangle \pm |-2\rangle)/\sqrt{2}$ and $|\pm J\rangle = (|+2\rangle \pm j|-2\rangle)/\sqrt{2})$. To build the projection technique, we design the metasurface that should have the OAM, polarization, and path multiplexing function (Figure 1a), which is composed of subwavelength elliptical pillars with two independently adjustable structural parameters (D_x and D_y), a fixed height H, and a fixed period P (Figure 1b). Its elliptical cross section results in different effective refractive indices for two linear polarizations along the two crossed axes, which is the fundamental mechanism for achieving polarization multiplexing.

The linearly polarized light is incident on the elliptical pillar, which will produce polarization-dependent phase shifts depending on D_x and D_y. The phase shifts (Φ_x and Φ_y) and the transmittances (T_x and T_y) for the x- and y-polarization are simulated by the finite-difference time-domain method, in which the wavelength is chosen to be $\lambda = 1550$ nm, the period is set to $P = 850$ nm, and the structural parameters (D_x and D_y) range from 150 to 700 nm (Figure 2a). We find two groups (A and B) of meta-atoms with high transmittances, which provide two kinds of different scatters. When the height of all the elliptical pillars is $H = 940$ nm, the corresponding transmittances are higher than 90%. The phases Φ_x of groups A and B are constants independent of D_x and D_y for the x-polarization, and the difference between the two groups is π (Figure 2b). Based on this property, we can construct a binary meta-vortex-grating for the $|H\rangle$-polarized light. In this case, we can change D_x and D_y in groups A and B by maintaining the binary grating for x-polarization. As shown in Figure 2b, another property of groups A and B is that the phases Φ_y can cover approximately a range of $[0, 2\pi]$ for y-polarization, which provide us the ability to construct the sine/cosine meta-vortex grating for the $|V\rangle$-polarized light by choosing the suitable meta-atom (see Note S2 in the Supporting Information).

The metasurface we designed is regarded as a meta-vortex-grating formed by elliptical pillars arranged based on the above principle. It has the projection functions of OAM states, depending on the polarization states of $|H\rangle$ and $|V\rangle$ (Figure S1) as

$$M_H \propto e^{-jk_x x}|-2\rangle + e^{jk_x x}|+2\rangle \quad M_V \propto e^{-jk_x x}|+J\rangle + e^{jk_x x}|+\rangle \quad (2)$$

where $\pm k_x$ are horizontal wave vectors, which indicate that the input light is diffracted into the two spatially separated channels (Path1 and Path2). We fabricate the silicon-based metasurface and experimentally verify its performance with classical light (Figure S2). The measured transmission

https://doi.org/10.1021/acs.nanolett.3c00554
Nano Lett. 2023, 23, 3921−3928

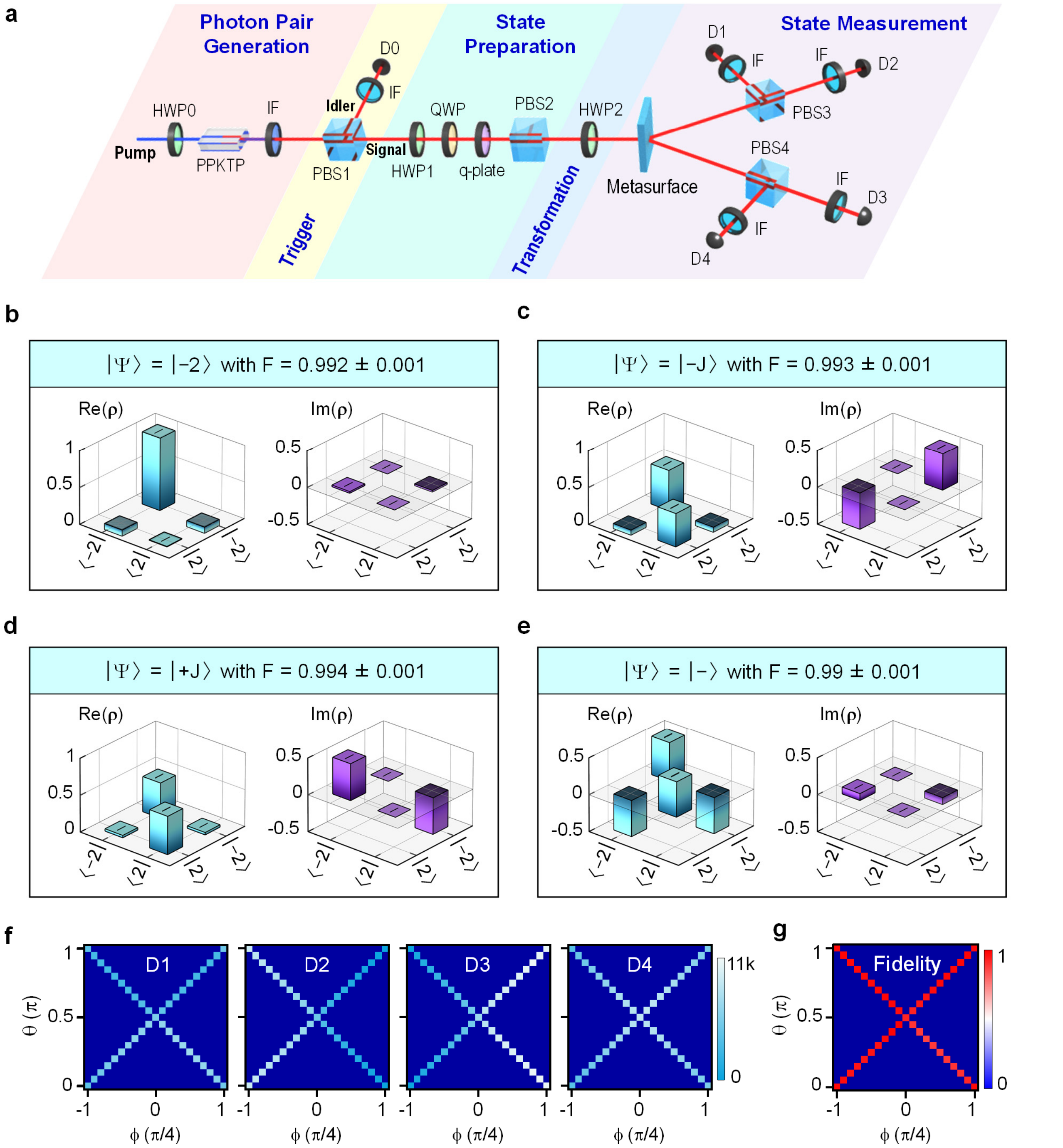

Figure 4. Experimental OAM quantum state reconstruction with the metasurface. (a) Schematic of the experimental setup. The SPDC process produces two photons, one in vertical polarization (V) and the other in horizontal polarization (H), centered at the degenerate wavelength of λ = 1550 nm. The pump and photons produced at other wavelengths are filtered by an interference filter (IF). The photon pairs produced by the SPDC are spatially separated by using a polarizing beam splitter (PBS1). The reflected photons act as a trigger for the detection of the "signal photons". The signal photons are passed through the optical components (HWP1, QWP, q-plate, and PBS2) for the generation of the prepared state. In the measurement process, HWP2 is used to control the polarization of the OAM state, and then the signal photons are projected into different OAM bases by the metasurface. Coincidence counts between the trigger D0 and the superconducting single-photon detectors D1−D4 are used to reconstruct the density matrix. (b−e) Experimentally measured density matrices of the single-photon OAM state of $|-2\rangle$, $|-J\rangle$, $|+J\rangle$, and $|-\rangle$, respectively. (f) Measured coincidence counts between the trigger (D0) and the superconducting single-photon detectors D1−D4 for other OAM states with different combinations of θ and ϕ in eq 1. (g) Fidelities of the measured OAM states corresponding to (f).

efficiency is close to 90% for horizontally and vertically polarized light. After projecting by the metasurface, the detector can only detect the input OAM state that can be converted into a fundamental Gaussian mode due to the filter of a single-mode fiber (SMF). The measured results are shown in Figure 3 for six different input OAM states. With eq 2, for the $|H\rangle$-polarized light, the input state of $|-2\rangle$ ($|+2\rangle$) will be projected by the metasurface into the Gaussian mode in Path1 (Path2), as shown in Figure 3a (Figure 3b). For the $|V\rangle$-polarized light, the input state of $|-J\rangle$ ($|-\rangle$) will be projected

https://doi.org/10.1021/acs.nanolett.3c00554
Nano Lett. 2023, 23, 3921−3928

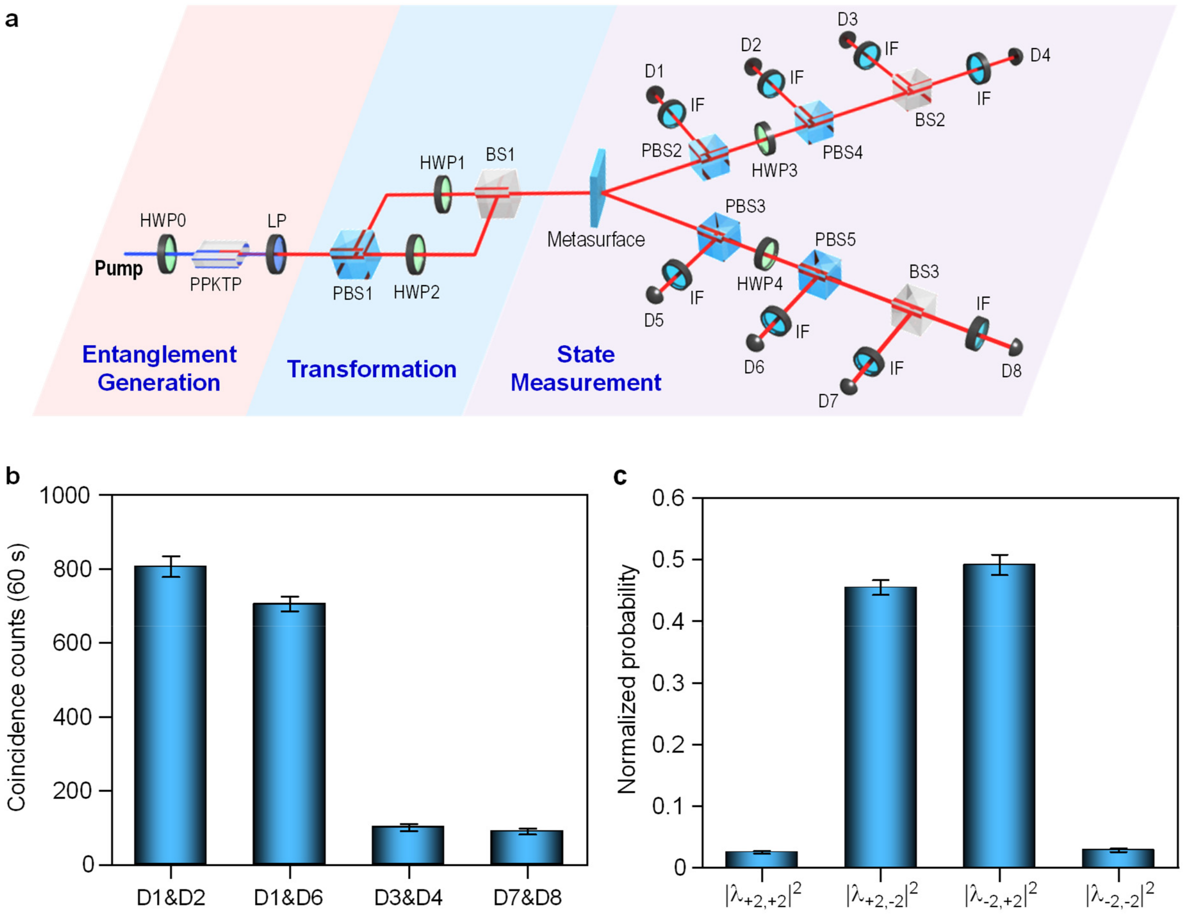

Figure 5. Setup and measurements for calculating the Schmidt number of the OAM entanglement. (a) A 775 nm diode laser pumps the PPKTP crystal phase-matched for collinear type-II SPDC, which produces the OAM entanglement at the degenerate wavelength of λ = 1550 nm, filtered with IF of $\Delta\lambda$ = 10 nm. After PBS1, the polarizations of the signal and idler photons are controlled by HWP1 and HWP2, respectively. Two photons are combined into one path by BS1 and enter the metasurface. Coincidence counts between the superconducting single-photon detectors are used to measure the Schmidt number of the OAM entangled state $|\Phi^+\rangle = (|+2\rangle_s|-2\rangle_i + |-2\rangle_s\,|+2\rangle_i)/\sqrt{2}$. (b) Measured coincidence counts behind the metasurface. (c) Calculated coincidence probability.

into the Gaussian mode in Path1 (Path2), as shown in Figure 3c (Figure 3d), but the intensity is only half of that in the case in Figure 3a (Figure 3b), because of the orthogonality with the state of $|+J\rangle$ ($|+\rangle$). In contrast, the metasurface converts the input $|V\rangle$-polarized state of $|+\rangle$ into the Gaussian modes in both Path1 and Path2, but the intensity in Path2 is about half of that in Path1, as shown in Figure 3e. For the input $|V\rangle$-polarized state of $|+J\rangle$, although the situation is similar to the case of $|+\rangle$, the intensity distributions in Path1 and Path2 are reversed, as shown in Figure 3f. Obviously, the metasurface we designed and fabricated has a good performance, as predicted in theory. The measured diffraction efficiency is 23% for horizontal polarization and 19% for vertical polarization.

We realize an application of the multiplexing metasurface for the measurement of the single-photon OAM quantum state. The tomography requires the measurements performed in four different projective bases: two orthogonal bases of $|\pm 2\rangle$ and two additional bases of $|+\rangle$ and $|+J\rangle$. This sequence of measurement allows us to perform the reconstruction of the density matrix of any single-photon OAM quantum state with $|m| = 2$, which can be generally expressed as

$$\rho = \frac{1}{2}\sum_{i=0}^{3} S_i\hat{\sigma}_i \tag{3}$$

where $\hat{\sigma}_i$ are the Pauli matrices and S_i are called the Stokes parameters of the OAM state,[41] which may be identified experimentally via the above four OAM projections with $S_i = 2P_i/P_0 - 1$ (i = 0, ..., 3), P_0 is the total probability, and P_1, P_2, and P_3 correspond to the probabilities of the single-photon OAM states. Figure 4a shows the experimental setup to generate and measure the single-photon OAM state. A heralded single-photon source at a wavelength of 1550 nm is generated from the SPDC process in the PPKTP nonlinear crystal (see Note S4 in the Supporting Information). They are prepared in different OAM states by using a quarter-wave plate (QWP), a half-wave plate (HWP1), and a q-plate and then sent to the metasurface. The photons diffracted by the metasurface are collected and detected by the superconducting single-photon (SC-SP) detector with the SMF pigtail. By measuring the correlations with the trigger SC-SP detector (D0), we reconstruct the OAM state from the photon counts at the four ports D1−D4. We experimentally recover the density matrices of four OAM states of $|-2\rangle$, $|-J\rangle$, $|+J\rangle$, and $|-\rangle$ with fidelities of 0.992 ± 0.001, 0.993 ± 0.001, 0.994 ± 0.001 and 0.990 ± 0.001, respectively (see Figure 4b−e), where we define the fidelity between the recovered ρ_e and theoretical density matrices ρ_t by $F(\rho_t, \rho_e) = \mathrm{Tr}(\sqrt{\sqrt{\rho_t}\rho_e\sqrt{\rho_t}})^2$. These results are in very good agreement with theory. In addition, we

https://doi.org/10.1021/acs.nanolett.3c00554
Nano Lett. 2023, 23, 3921−3928

measure the various OAM states located on the Viviani curve on the Bloch sphere (Figure S3). The coincidence counts between the trigger D0 and four SC-SP detectors D1−D4 for the states with different combinations of θ and ϕ in eq 1 are shown in Figure 4f, and the reconstructed states present a fidelity higher than 0.871 with respect to the prepared states (see Figure 4g and Figure S3).

Entanglement is an important resource, which allows the quantum technology to be beyond the classical one possible. The certification and quantification of entanglement is a crucial task because maximally entangled pure states will become nonmaximally entangled or partially mixed states due to the dissipation and decoherence. The full state tomography is a feasible solution for this task,[42] but the experimental measurement is too complex. The two-photon OAM pure states, separable or entangled, can be Schmidt decomposed into

$$|\Psi\rangle = \sum_{m=-\infty}^{\infty} \lambda_m |m\rangle \otimes |-m\rangle \quad (4)$$

where the coefficient $\lambda_m(\lambda_{m_1,m_2}, m_1 = m, m_2 = -m)$ is the probability amplitude (satisfying the normalization condition, $\Sigma|\lambda_{m_1,m_2}|^2 = 1$) of finding the signal photon with the OAM of $m_1\hbar$ and the idler photon with the OAM of $m_2\hbar$ in coincidence. The Schmidt number is often defined as $K = 1/\sum|\lambda_{m_1,m_2}|^4$ to evaluate the effective dimensionality of the system because it represents the minimum local Hilbert space dimension required to faithfully represent the correlation of the quantum state.[43,44]

One main approach for the measurement of probability is to sequentially display the specific hologram onto two separated SLMs for the given input OAM modes of the signal and idler photons, respectively, and then measure its correlation by the single-photon detectors. However, this method is very inefficient because we must change the hologram on the SLM to scan the projective basis. Here we use only a single metasurface with the OAM, polarization, and path multiplexing function to measure $|\lambda_{m_1,m_2}|^2$, as shown in Figure 5a. The photon pairs from the type-II phase-matched SPDC process in the PPKTP crystal are separated by PBS1 to two paths. By using HWP1 and HWP2, the Bell state $|\Phi^+\rangle = (|+2\rangle_s|-2\rangle_i + |-2\rangle_s|+2\rangle_i)/\sqrt{2}$ can be generated with the same horizontal polarization. To use only the single metasurface and take the full advantages of the multiplexing property, we need to control the polarization states of photons in two paths by HWP1 and HWP2, respectively, and then combine them into one path with BS1 to enter the metasurface. To avoid the Hong−Ou−Mandel interference on BS1, we introduce a small time delay (not shown in Figure 5a) between two paths, and it will be compensated at the detection stage. Projecting by the metasurface, the photons go to different detectors, which are determined by HWPs (HWP3 and HWP4), PBSs (PBS2−PBS5) and BSs (BS2 and BS3), for coincidence measurement. When the orientation angles of the fast axis of HWPs (HWP1−HWP4) with respect to the horizontal direction are $\alpha_1 = \pi/4$ and $\alpha_2 = \alpha_3 = \alpha_4 = 0$, we can obtain the probabilities of $|\lambda_{+2,+2}|^2 = 4C_{D7\otimes D8}$ and $|\lambda_{-2,-2}|^2 = 4C_{D3\otimes D4}$ from the coincidence counts between different detectors $C_{D_i\otimes D_j}$ (see Note S6 in the Supporting Information). Then tuning the orientation angles of HWPs to $\alpha_1 = \alpha_2 = 0$ and $\alpha_3 = \alpha_4 = \pi/4$, we can calculate another two probabilities of $|\lambda_{+2,-2}|^2 = 4(C_{D1\otimes D6} - C_{D7\otimes D8})$ and $|\lambda_{-2,+2}|^2 = 4(C_{D1\otimes D2} - C_{D3\otimes D4})$ (see Note S6 in the Supporting Information). Figure 5b shows the experimental results of the coincidences. Considering the loss from the metasurface, we obtain the normalized probabilities (Figure 5c). In this way, the Schmidt number is $K = 1.991 \pm 0.001$, which is close to 2, the Schmidt number of the maximum entangled state, showing that our system is almost the pure two-dimensional OAM entangled state.

In conclusion, we have demonstrated a multiparameter and multiplexing metasurface designed based on the birefringent property of the meta-atoms, enabling the measurement of the OAM quantum state of photons, which paves the way for nanophotonic quantum information applications. This provides a miniatured and stable solution for the quantum measurement with high accuracy and efficiency, as we have reconstructed experimentally the density matrix of the single-photon OAM states and obtained the Schmidt number of the OAM entangled state. The all-dielectric platform not only makes us free from the deposition of additional materials but also provides us a straightforward and practical way to achieve on-demand phase control, because of only one-step fabrication and easier integration with the current CMOS technology. We anticipate that the birefringent metasurface will become an integrated tool in quantum optics and will be used widely in photonic quantum information systems—for example, for performing state tomography. This idea can be extended to implement the measurement of high-dimensional OAM quantum states by using multipath metasurfaces for applications in free-space communications, multichannel information processing, and quantum imaging.

■ METHODS

Sample Fabrication. The fabrication of the proposed metasurface started with acetone/isopropyl alcohol/deionized water cleaning of a slide glass to promote the adhesion between the a-Si:H film and the glass substrate. Then a 940 nm thick a-Si:H film was deposited onto the substrate via plasma-enhanced chemical vapor deposition (Plasmalab 100 from Oxford). After spin coating of an electron beam resist (ZEP520A from Zeon Chemicals), a thin layer of e-spacer 300Z (Showa Denko) was coated to avoid charging during subsequent electron beam exposure. The metasurface pattern was then formed using an electron beam writer (Raith150) and development in ZED-N50. Next, a 60 nm thick Al layer was deposited by e-beam evaporation (Temescal BJD-2000), followed by a lift-off process by soaking the sample in a resist remover (ZDMAC from Zeon Co.). The remaining oval-shaped Al pattern array was used as an etch mask to transfer the designed pattern into the a-Si:H film through fluorine-based inductively coupled plasma-reactive ion etching (Oxford Plasmalab System 100). Finally, the residual Al etch mask was removed by Al wet etchant.

Numerical Simulations. Numerical simulations were conducted by using 3D finite-difference time-domain (FDTD) simulations. For unit cell (meta-atom) design, a-Si:H elliptical nanopillars with a fixed height of 940 nm, arranged on a hexagonal lattice with a lattice constant of 850 nm, were sited on a glass substrate. To obtain the database of the building blocks used in metadevice design, periodic boundary conditions were applied along both the x-and y-axes, while perfectly matched layer (PML) boundary conditions were imposed along the z-axis. The unit cells were illuminated by a plane wave source polarized along x- or

y-axes at λ = 1550 nm, which was positioned inside the substrate. The transmittances (T_x and T_y) and the corresponding phase shifts (Φ_x and Φ_y) were obtained by sweeping the lateral dimensions (D_x and D_y) of the nanopillars from 150 to 700 nm, respectively, as shown in Figure 2a. The intensities of the transmitted wave in two paths of the metasurface for different polarizations were recorded through a power monitor (in the x−y plane) positioned in the air above the metasurface. Subsequently, the multiplexing metasurface could be constructed by choosing the optimized birefringent meta-atoms from the database for each (x, y), as shown in Figure 2b.

■ ASSOCIATED CONTENT

Supporting Information

The Supporting Information is available free of charge at https://pubs.acs.org/doi/10.1021/acs.nanolett.3c00554.

Additional notes and figures, including the OAM states on the Bloch sphere measured based on the multiplexing metasurface, a sketch of the characterization of the multiplexing metasurface performance and the experimental setup of the metasurface measurement using classical light, preparation of the SPDC source, the fidelities of reconstructed density matrices, and the calculation of the coincidence of a two-photon OAM entangled state (PDF)

■ AUTHOR INFORMATION

Corresponding Authors

Yongnan Li − *The Key Laboratory of Weak Light Nonlinear Photonics, Ministry of Education, School of Physics, Nankai University, Tianjin 300071, People's Republic of China;* orcid.org/0000-0003-1607-7486; Email: liyongnan@nankai.edu.cn

Shuqi Chen − *The Key Laboratory of Weak Light Nonlinear Photonics, Ministry of Education, School of Physics and School of TEDA Institute of Applied Physics, Nankai University, Tianjin 300071, People's Republic of China; The Collaborative Innovation Center of Extreme Optics, Shanxi University, Taiyuan, Shanxi 030006, People's Republic of China;* orcid.org/0000-0002-7898-4148; Email: schen@nankai.edu.cn

Hui-Tian Wang − *National Laboratory of Solid State Microstructures and School of Physics, Collaborative Innovation Center of Advanced Microstructures, Nanjing University, Nanjing 210093, People's Republic of China; The Collaborative Innovation Center of Extreme Optics, Shanxi University, Taiyuan, Shanxi 030006, People's Republic of China*; Email: htwang@nju.edu.cn

Authors

Min Wang − *The Key Laboratory of Weak Light Nonlinear Photonics, Ministry of Education, School of Physics, Nankai University, Tianjin 300071, People's Republic of China*

Lieyu Chen − *The Key Laboratory of Weak Light Nonlinear Photonics, Ministry of Education, School of Physics, Nankai University, Tianjin 300071, People's Republic of China*

Duk-Yong Choi − *Laser Physics Centre, Research School of Physics and Engineering, Australian National University, Canberra, Australian Central Territory 2601, Australia; College of Information Science and Technology, Jinan University, Guangzhou 510632, People's Republic of China;* orcid.org/0000-0002-5339-3085

Shuangyin Huang − *National Laboratory of Solid State Microstructures and School of Physics, Collaborative Innovation Center of Advanced Microstructures, Nanjing University, Nanjing 210093, People's Republic of China*

Qiang Wang − *The Key Laboratory of Weak Light Nonlinear Photonics, Ministry of Education, School of Physics, Nankai University, Tianjin 300071, People's Republic of China*

Chenghou Tu − *The Key Laboratory of Weak Light Nonlinear Photonics, Ministry of Education, School of Physics, Nankai University, Tianjin 300071, People's Republic of China*

Hua Cheng − *The Key Laboratory of Weak Light Nonlinear Photonics, Ministry of Education, School of Physics, Nankai University, Tianjin 300071, People's Republic of China*

Jianguo Tian − *The Key Laboratory of Weak Light Nonlinear Photonics, Ministry of Education, School of Physics, Nankai University, Tianjin 300071, People's Republic of China*

Complete contact information is available at: https://pubs.acs.org/10.1021/acs.nanolett.3c00554

Author Contributions

M.W. and L.C. contributed equally to this work. M.W. and L.C. designed and performed the measurements, analyzed the data, and wrote the manuscript. D.-Y.C. fabricated the devices. All the authors contributed to the analyses and discussions of the manuscript. Y.L., S.C., and H.W. supervised, designed the study, and wrote the manuscript.

Notes

The authors declare no competing financial interest.

■ ACKNOWLEDGMENTS

This work was supported by the National Key Research and Development Program of China (2021YFA1400601 and 2022YFA1404501), the National Natural Science Fund for Distinguished Young Scholars (11925403), and the National Natural Science Foundation of China (12234009, 12122406, 12192253, 12074197, and 11974193). The metasurface nanofabrication was performed at the ACT node of the Australian National Fabrication Facility.

■ REFERENCES

(1) Kildishev, A. V.; Boltasseva, A.; Shalaev, V. M. Planar photonics with metasurfaces. *Science* **2013**, *339*, 1232009.

(2) Chen, H.-T.; Taylor, A. J.; Yu, N. A Review of Metasurfaces: Physics and Applications. *Rep. Prog. Phys.* **2016**, *79*, 076401.

(3) Shaltout, A. M.; Shalaev, V. M.; Brongersma, M. L. Spatiotemporal light control with active metasurfaces. *Science* **2019**, *364*, eaat3100.

(4) Balthasar Mueller, J. P.; Rubin, N. A.; Devlin, R. C.; Groever, B.; Capasso, F. Metasurface polarization optics: independent phase control of arbitrary orthogonal states of polarization. *Phys. Rev. Lett.* **2017**, *118*, 113901.

(5) Devlin, R. C.; Ambrosio, A.; Rubin, N. A.; Mueller, J. B.; Capasso, F. Arbitrary spin-to−orbital angular momentum conversion of light. *Science* **2017**, *358*, 896−901.

(6) High, A. A.; Devlin, R. C.; Dibos, A.; Polking, M.; Wild, D. S.; Perczel, J.; de Leon, N. P.; Lukin, M. D.; Park, H. Visible-frequency hyperbolic metasurface. *Nature* **2015**, *522*, 192−196.

(7) Ra'di, Y.; Sounas, D. L.; Alù, A. Metagratings: Beyond the Limits of Graded Metasurfaces for Wave Front Control. *Phys. Rev. Lett.* **2017**, *119*, 067404.

(8) Khorasaninejad, M.; Capasso, F. Metalenses: Versatile multifunctional photonic components. *Science* **2017**, *358*, 1146.

(9) Tittl, A.; Leitis, A.; Liu, M.; Yesilkoy, F.; Choi, D.-Y.; Neshev, D. N.; Kivshar, Y. S.; Altug, H. Imaging-based molecular barcoding with pixelated dielectric metasurfaces. *Science* **2018**, *360*, 1105−1109.
(10) Arbabi, A.; Arbabi, E.; Kamali, S. M.; Horie, Y.; Han, S.; Faraon, A. Miniature optical planar camera based on a wide-angle metasurface doublet corrected for monochromatic aberrations. *Nat. Commun.* **2016**, *7*, 13682.
(11) Colburn, S.; Zhan, A.; Majumdar, A. Metasurface optics for full-color computational imaging. *Sci. Adv.* **2018**, *4*, eaar2114.
(12) Zheng, G.; Mühlenbernd, H.; Kenney, M.; Li, G.; Zentgraf, T.; Zhang, S. Metasurface holograms reaching 80% efficiency. *Nat. Nanotechnol.* **2015**, *10*, 308−312.
(13) Huang, L.; Chen, X.; Mühlenbernd, H.; Zhang, H.; Chen, S.; Bai, B.; Tan, Q.; Jin, G.; Cheah, K.-W.; Qiu, C.-W.; Li, J.; Zentgraf, T.; Zhang, S. Three-dimensional optical holography using a plasmonic metasurface. *Nat. Commun.* **2013**, *4*, 2808.
(14) Ren, H.; Briere, G.; Fang, X.; Ni, P.; Sawant, R.; Héron, S.; Chenot, S.; Vézian, S.; Damilano, B.; Brandli, V.; Maier, S. A.; Genevet, P. Metasurface orbital angular momentum Holography. *Nat. Commun.* **2019**, *10*, 2986.
(15) Ren, H.; Fang, X.; Jang, J.; Burger, J.; Rho, J.; Maier, S. A. Complex-amplitude metasurface-based orbital angular momentum holography in momentum space. *Nat. Nanotechnol.* **2020**, *15*, 948−955.
(16) Ni, X.; Wong, Z. J.; Mrejen, M.; Wang, Y.; Zhang, X. An ultrathin invisibility skin cloak for visible light. *Science* **2015**, *349*, 1310−1314.
(17) Yang, Y.; Jing, L.; Zheng, B.; Hao, R.; Yin, W.; Li, E.; Soukoulis, C. M.; Chen, H. Full-Polarization 3D Metasurface Cloak with Preserved Amplitude and Phase. *Adv. Mater.* **2016**, *28*, 6866−6871.
(18) Ye, W.; Zeuner, F.; Li, X.; Reineke, B.; He, S.; Qiu, C.-W.; Liu, J.; Wang, Y.; Zhang, S.; Zentgraf, T. Spin and wavelength multiplexed nonlinear metasurface holography. *Nat. Commun.* **2016**, *7*, 11930.
(19) Lee, J.; Tymchenko, M.; Argyropoulos, C.; Chen, P.-Y.; Lu, F.; Demmerle, F.; Boehm, G.; Amann, M.-C.; Alù, A.; Belkin, M. A. Giant nonlinear response from plasmonic metasurfaces coupled to intersubband transitions. *Nature* **2014**, *511*, 65−69.
(20) Minovich, A. E.; Miroshnichenko, A. E.; Bykov, A. Y.; Murzina, T. V.; Neshev, D. N.; Kivshar, Y. S. Functional and nonlinear optical metasurfaces. *Laser Photonics Rev.* **2015**, *9*, 195−213.
(21) Solntsev, A. S.; Agarwal, G. S.; Kivshar, Y. S. Metasurfaces for quantum photonics. *Nat. Photonics* **2021**, *15*, 327−336.
(22) Liu, J.; Shi, M.; Chen, Z.; Wang, S.; Wang, Z.; Zhu, S. Quantum photonics based on metasurfaces. *OptoElectron. Adv.* **2021**, *4*, 200092.
(23) Li, L.; Liu, Z.; Ren, X.; Wang, S.; Su, V.; Chen, M.; Chu, C. H.; Kuo, H. Y.; Liu, B.; Zang, W.; Guo, G.; Zhang, L.; Wang, Z.; Zhu, S.; Tsai, D. P. Metalens-array−based high-dimensional and multiphoton quantum source. *Science* **2020**, *368*, 1487−1490.
(24) Stav, T.; Faerman, A.; Maguid, E.; Oren, D.; Kleiner, V.; Hasman, E.; Segev, M. Quantum entanglement of the spin and orbital angular momentum of photons using metamaterials. *Science* **2018**, *361*, 1101−1104.
(25) Wang, K.; Titchener, J. G.; Kruk, S. S.; Xu, L.; Chung, H.-P.; Parry, M.; Kravchenko, I. I.; Chen, Y.-H.; Solntsev, A. S.; Kivshar, Y. S.; Neshev, D. N.; Sukhorukov, A. A. Quantum metasurface for multiphoton interference and state reconstruction. *Science* **2018**, *361*, 1104−1108.
(26) Chen, S.; Liu, W.; Li, Z.; Cheng, H.; Tian, J. Metasurface-Empowered Optical Multiplexing and Multifunction. *Adv. Mater.* **2020**, *32*, 1805912.
(27) Arbabi, A.; Horie, Y.; Bagheri, M.; Faraon, A. Dielectric metasurfaces for complete control of phase and polarization with subwavelength spatial resolution and high transmission. *Nat. Nanotechnol.* **2015**, *10*, 937−943.
(28) Mehmood, M. Q.; Mei, S.; Hussain, S.; Huang, K.; Siew, S. Y.; Zhang, L.; Zhang, T.; Ling, X.; Liu, H.; Teng, J.; Danner, A.; Zhang, S.; Qiu, C.-W. Visible-Frequency Metasurface for Structuring and Spatially Multiplexing Optical Vortices. *Adv. Mater.* **2016**, *28*, 2533−2539.
(29) Erhard, M.; Fickler, R.; Krenn, M.; Zeilinger, A. Twisted photons: new quantum perspectives in high Dimensions. *Light Sci. Appl.* **2018**, *7*, 17146−17146.
(30) Erhard, M.; Krenn, M.; Zeilinger, A. Advances in high-dimensional quantum entanglement. *Nat. Rev. Phys.* **2020**, *2*, 365−381.
(31) Fickler, R.; Lapkiewicz, R.; Plick, W. N.; Krenn, M.; Schaeff, C.; Ramelow, S.; Zeilinger, A. Quantum Entanglement of High Angular Momenta. *Science* **2012**, *338*, 640−643.
(32) Mair, A.; Vaziri, A.; Weihs, G.; Zeilinger, A. Entanglement of the orbital angular momentum states of photons. *Nature* **2001**, *412*, 313−316.
(33) Kong, L.-J.; Liu, R.; Qi, W.-R.; Wang, Z.-X.; Huang, S.-Y.; Wang, Q.; Tu, C.; Li, Y.; Wang, H.-T. Manipulation of eight-dimensional Bell-like states. *Sci. Adv.* **2019**, *5*, eaat9206.
(34) Sit, A.; Bouchard, F.; Fickler, R.; Gagnon-Bischoff, J.; Larocque, H.; Heshami, K.; Elser, D.; Peuntinger, C.; Günthner, K.; Heim, B.; Marquardt, C.; Leuchs, G.; Boyd, R. W.; Karimi, E. High-dimensional intracity quantum cryptography with structured photons. *Optica* **2017**, *4*, 1006−1010.
(35) Vallone, G.; D'Ambrosio, V.; Sponselli, A.; Slussarenko, S.; Marrucci, L.; Sciarrino, F.; Villoresi, P. Free-Space Quantum Key Distribution by Rotation-Invariant Twisted Photons. *Phys. Rev. Lett.* **2014**, *113*, 060503.
(36) Krenn, M.; Handsteiner, J.; Fink, M.; Fickler, R.; Zeilinger, A. Twisted photon entanglement through turbulent air across Vienna. *Proc. Natl. Acad. Sci. U.S.A.* **2015**, *112*, 14197−14201.
(37) Krenn, M.; Malik, M.; Erhard, M.; Zeilinger, A. Orbital angular momentum of photons and the entanglement of Laguerre−Gaussian modes. *Philos. Trans. R. Soc. A* **2017**, *375*, 20150442.
(38) Li, Y.; Huang, S.-Y.; Wang, M.; Tu, C.; Wang, X.-L.; Li, Y.; Wang, H.-T. Two-Measurement Tomography of High-Dimensional Orbital Angular Momentum Entanglement. *Phys. Rev. Lett.* **2023**, *130*, 050805.
(39) Jack, B.; Leach, J.; Ritsch, H.; Barnett, S. M.; Padgett, M. J.; Franke-Arnold, S. Precise quantum tomography of photon pairs with entangled orbital angular momentum. *N. J. Phys.* **2009**, *11*, 103024.
(40) Jack, B.; Yao, A. M.; Leach, J.; Romero, J.; Franke-Arnold, S.; Ireland, D. G.; Barnett, S. M.; Padgett, M. J. Entanglement of arbitrary superpositions of modes within two-dimensional orbital angular momentum state spaces. *Phys. Rev. A* **2010**, *81*, 043844.
(41) Abouraddy, A. F.; Kagalwala, K. H.; Saleh, B. E. Two-point optical coherency matrix tomography. *Opt. Lett.* **2014**, *39*, 2411−2414.
(42) Kong, L. J.; Liu, R.; Qi, W. R.; Wang, Z. X.; Huang, S. Y.; Tu, C. H.; Li, Y. N.; Wang, H. T. Asymptotical Locking Tomography of High-Dimensional Entanglement. *Chin. Phys. Lett.* **2020**, *37*, 034204.
(43) Giovannini, D.; Miatto, F. M.; Romero, J.; Barnett, S. M.; Woerdman, J. P.; Padgett, M. J. Determining the dimensionality of bipartite orbital-angular-momentum entanglement using multi-sector phase masks. *New. J. Phys.* **2012**, *14*, 073046.
(44) Peeters, W. H.; Verstegen, E. J. K.; van Exter, M. P. Orbital angular momentum analysis of high-dimensional entanglement. *Phys. Rev. A* **2007**, *76*, 042302.

https://doi.org/10.1021/acs.nanolett.3c00554
Nano Lett. 2023, 23, 3921−3928